Numerical Heat Transfer, Part B, 57: 414–439, 2010
Copyright © Taylor & Francis Group, LLC
ISSN: 1040-7790 print/1521-0626 online
DOI: 10.1080/10407791003685155

ERROR ANALYSIS OF THE FINITE-VOLUME METHOD WITH RESPECT TO MESH TYPE

F. Juretić[1] and A. D. Gosman[2]
[1]*AVL-AST d.o.o, Zagreb, Croatia*
[2]*CD-Adapco Ltd., London, England*

This article presents truncation error terms for flux approximations on mesh faces, needed by the finite-volume method, and their influence on solution accuracy in the search for the optimal cell type. Face truncation errors are used to assemble truncation errors for different cell types such as squares, triangles, and hexagons. It is shown that squares have the smallest and triangles the largest truncation errors, for the same cell size, which is also confirmed by numerical experiments. It is also shown that polyhedral meshes consisting of hexagons are slightly less accurate than hexahedral meshes with the same cell size.

1. INTRODUCTION

The issue of numerical accuracy in computational fluid dynamics (CFD) is becoming very important as it becomes a widely used engineering tool. The method most widely used for solving fluid flow problems is the finite-volume method (FVM), whose accuracy is examined in this article.

The FVM is a well-established tool used for solving problems involving combustion [1–5], radiation [6–18], multiphase flow [19], flow in a porous medium [20], moving-boundary problems [21–24], biological processes [25], non-Newtonian flows [26], etc.

The finite-volume discretization of the partial differential equations is performed using the integral formulation of the conservation laws, such that the quantity of interest remains conserved. The solution domain is subdivided into contiguous control volumes (CVs), which can move in space with time but should not overlap. The older versions of the finite-volume methods, see Ferziger et al. [27], Versteeg et al. [28], Dong et al. [29], Lilek et al. [30] and many more, required so-called structured grids which consist of the same type of cells which are ordered in a systematic manner. However, structured grids are not suitable for geometries appearing in engineering practice, because it is hardly ever possible to generate meshes of good quality in complex geometries and refine them only where needed to achieve the required accuracy with a reasonable number of cells. The finite-volume

Received 11 March 2009; accepted 1 February 2010.
This work is a result of Franjo Juretic's Ph.D. research, which was sponsored by CD-Adapco Ltd.
Address correspondence to F. Juretić, AVL-AST d.o.o, Avenija Dubrovnik 10, Zagreb 10020, Croatia. E-mail: franjo.juretic@avl.com

NOMENCLATURE

CD	central differencing	Δ	orthogonal part of the face area vector
$C_p = p - p_{atm}/0.5pU$	pressure coefficient		
$\mathbf{d}$	$\overline{PN}$ vector	ϕ	general tensorial property
e	truncation error, discretization error	$\underline{\phi}$	approximated value of general tensorial property
f	face, face interpolate	ψ	measure of skewness
f_x	interpolation factor		
F	face convection flux	**Subscripts**	
FVM	finite-volume method	convHexagon	convection on hexagonal mesh
$\mathbf{k}$	nonorthogonal part of the face area vector	convSquare	convection on square mesh
$\hat{\mathbf{k}}$	nonorthogonal part of the face area unit vector	convTri	convection on triangular mesh
l	side length		
$\mathbf{m}$	skewness vector	CV	control volume
$\hat{\mathbf{m}}$	skewness unit vector	diff	diffusion
$\mathbf{n}$	unit normal vector	diffHexagon	diffusion on hexagonal mesh
Re	Reynolds numbe		
S	area vector	diffSquare	diffusion on square mesh
ΔS	sum of face area vectors on two faces	diffTri	diffusion on triangular mesh
S(x, ϕ)	source term	f	face center
Sp (x_P, ϕ_P)	implicit part of the source term	f_i	intersection of face with vector $\overline{PN}$
Su (x_P, ϕ_P)	explicit part of the source term	i	label of the current cell
U	velocity	interpolation	linear interpolation for skewed meshes
ΔU	difference of transport velocities on two faces	l	linear interpolation
UD	upwind differencing	mean	mean, average
V	volume	N	center of the neighboring control volume
x	position vector	P	center of the control volume
α	flow angle		
α_N	nonorthogonality angle	sng	surface-normal gradient
Γ_ϕ	diffusivity	source	source term

methods which operate on cells of arbitrary shape are becoming very popular [27, 31–37] because the cells of arbitrary topology make the process of mesh generation in complex domains easier.

The discretization error is an important class of errors in the FVM solution which are the main interest of this work. There have been several attempts at estimating the discretization error; see [32, 33, 38–41]. The information about the discretization error can also be used to drive the mesh refinement in order to control the discretization accuracy; see [33, 40–43] and others.

Perez-Segarra et al. [44] and Farre et al. [45] have performed an analysis of various discretization schemes which included the influence of the solution type and the mesh quality on the accuracy of various terms. However, they did not analyze the influence of different types of cells on the solution error.

This article provides the truncation error terms for convection and diffusion terms for different shapes of control volumes in two dimensions, i.e., squares, triangles, and hexagons, in a search for the optimal cell type. Triangles and squares are considered because they are common types of cells, while hexagons can be created automatically as a dual of a Delaunay triangulation. Examples of hexagonal meshes can be found in [35, 40, 46–48].

The article is organized as follows. Section 2 presents the finite-volume discretization with polyhedral mesh support and the truncation errors for face flux approximations. Truncation errors for the convection and diffusion terms are assembled in Section 3. Numerical examples illustrating the behavior of the discretization error on two laminar flow examples are shown in Section 4. The findings of the work are analyzed in Section 5.

2. FINITE-VOLUME DISCRETIZATION

A short outline of the finite-volume discretization on polyhedral meshes will be given in this section.

The finite-volume discretization consists of two consecutive steps. The first step is to decompose the domain into convex polyhedra, see Figure 1, which cover the whole domain and do not overlap.

The second step is the discretization of the governing partial differential equations on the given mesh. A steady-state transport equation for a tensorial property ϕ is used as an example for presenting FV discretization and truncation error analysis in this work. It has the following form:

$$\nabla \cdot (\mathbf{U}\phi) - \nabla \cdot (\Gamma_\phi \nabla \phi) = \mathbf{S}(\mathbf{x}, \phi) \tag{1}$$

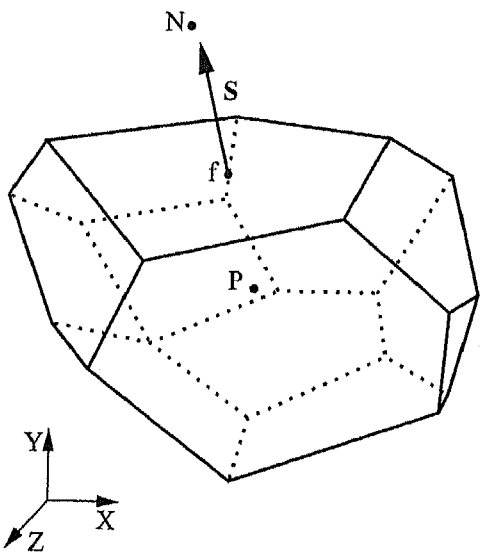

Figure 1. Control volume.

where $\mathbf{U}$ is the transport velocity and Γ_ϕ is the diffusion coefficient. The source term $S(x, \phi)$ is linearized [49]:

$$\mathbf{S}(\mathbf{x}, \phi) = Su(\mathbf{x}_P, \phi_P) + Sp(\mathbf{x}_P, \phi_P)\phi_P \tag{2}$$

The finite-volume discretization is performed using the integral form of Eq. (1):

$$\int_{V_{cv}} \nabla\cdot(\mathbf{U}\phi)dV - \int_{V_{cv}} \nabla\cdot(\Gamma_\phi \nabla\phi)\, dV = \int_{V_{cv}} \mathbf{S}(\mathbf{x}, \phi)dV \tag{3}$$

By assuming linear variation of ϕ in the control volume,

$$\phi = \phi_P + (\mathbf{x} - \mathbf{x}_P)\cdot(\nabla\phi)_P \tag{4}$$

we obtain second-order-accurate approximations for surface and volume integrals:

$$\int_{S_f} \phi|d\mathbf{S}| = \int_{S_f} [\phi_f + (\mathbf{x} - \mathbf{x}_f)\cdot(\nabla\phi)_P]\,|d\mathbf{S}| = \phi_f|\mathbf{S}_f| + O[(\mathbf{x} - \mathbf{x}_f)^2] \tag{5}$$

and

$$\int_{V_P} \phi\, dV = \int_{V_P} [\phi_P + (\mathbf{x} - \mathbf{x}_P)\cdot(\nabla\phi)_P]\, dV = \phi_P\, V_P + O[(\mathbf{x} - \mathbf{x}_P)^2] \tag{6}$$

respectively.

When the divergence terms in Eq. (3) are tranformed into sums of surface integrals using the Gauss theorem, and by using the above expressions for face and cell integrals, the discrete form of the transport equation is obtained:

$$\sum_f F\phi_f - \sum_f (\Gamma_\phi)_f(\mathbf{S}\cdot\nabla\phi)_f = \mathrm{Su}\ V_P + \mathrm{Sp}\phi_P\ V_P \tag{7}$$

where F is the face flux, defined as

$$F = \mathbf{U}_f \cdot \mathbf{S}_f \tag{8}$$

In order to complete the discretization process, the approximations for face value ϕ_f and face-normal gradient $(\mathbf{S}\cdot\nabla\phi)_f$ are still required. These terms are evaluated from the values in the neighboring cells, and their accuracy depends on the cell size and mesh quality. Properties which measure mesh quality are defined on mesh faces and as such do not depend on the shapes of the control volumes. The properties and their measures are as follows.

1. **Nonorthogonality** is measured by the angle a_N between the vector $\mathbf{d}$ and the face area vector $\mathbf{S}$; see Figure 2*a*. The vector $\mathbf{d}$ is defined as

$$\mathbf{d} = \mathbf{x}_N - \mathbf{x}_P \tag{9}$$

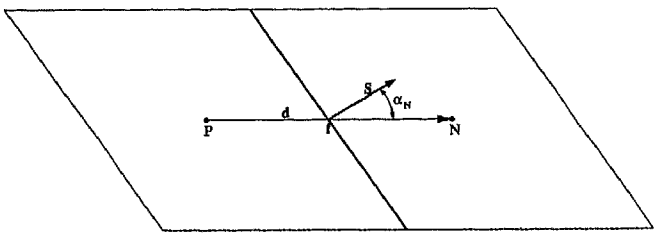

(*a*) Non-orthogonality

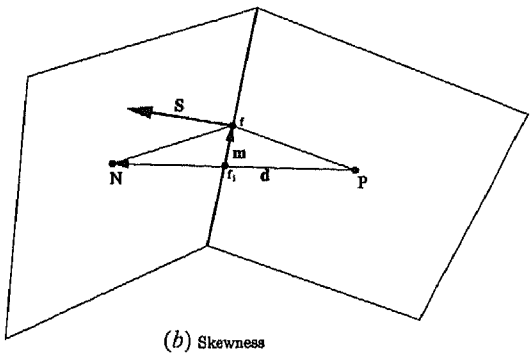

(*b*) Skewness

Figure 2. Mesh quality measures.

The angle should be as small as possible. The reasons for this will be given later in this section.

2. **Mesh skewness.** When the vector **d** does not intersect a face in its center, the mesh is defined as skewed (Figure 2*b*). The degree of skewness can be measured by

$$\psi = \frac{|\mathbf{m}|}{|\mathbf{d}|} \tag{10}$$

Here **m** is defined as

$$\mathbf{m} = \mathbf{x}_f - \mathbf{x}_{f_i} \tag{11}$$

where $\mathbf{x}_{f_i}$ denotes a point at which the vector **d** intersects the face (see Figure 2*b*). Skewness affects the accuracy of the interpolation from the nodes onto the faces, as will be shown in the remainder of the section.

3. **Uniformity.** A mesh is uniform when **d** intersects the face midway between the nodes P and N (Figure 2*b*). Uniformity can be measured by

$$f_x = \frac{|\mathbf{x}_{fi} - \mathbf{x}_N|}{|\mathbf{d}|} \tag{12}$$

thus $f_x = 0.5$ on uniform meshes. This property affects the accuracy of face-normal gradients.

The discretization procedures for the terms in the transport equation, Eq. (1), and their corresponding truncations errors will be presented term by term.

2.1. Convection Term

The discrete form of the convection term is

$$\sum_f F\underline{\phi_f} + e_{\text{conv}} \tag{13}$$

where the second-order-accurate value at the face ϕ_f is evaluated using a linear interpolation scheme [30]:

$$\underline{\phi_f} = (\underline{\phi_{f_i}} + \mathbf{m} \cdot \underline{(\nabla\phi)_{f_i}}) + e_{\text{interpolation}} \tag{14}$$

where $\underline{(\nabla\phi)_{f_i}}$ is the gradient interpolated at the face using:

$$\underline{\phi_{f_i}} = f_x\phi_P + (1 - f_x)\phi_N \tag{15}$$

$$\underline{(\nabla\phi)_{f_i}} = f_x(\nabla\phi)_P + (1 - f_x)(\nabla\phi)_N \tag{16}$$

The truncation error for the above interpolation practice can be estimated by using the following Taylor expansions:

$$\phi_P = \phi_{f_i} + (\mathbf{x}_P - \mathbf{x}_{f_i}) \cdot (\nabla\phi)_{f_i} + \frac{1}{2}(\mathbf{x}_P - \mathbf{x}_{f_i})^2 : (\nabla\nabla\phi)_{f_i} + \text{HOT} \tag{17}$$

$$\phi_N = \phi_{f_i} + (\mathbf{x}_N - \mathbf{x}_{f_i}) \cdot (\nabla\phi)_{f_i} + \frac{1}{2}(\mathbf{x}_N - \mathbf{x}_{f_i})^2 : (\nabla\nabla\phi)_{f_i} + \text{HOT} \tag{18}$$

$$\phi_f = \phi_{f_i} + \mathbf{m} \cdot (\nabla\phi)_{f_i} + \frac{1}{2}\mathbf{m}^2 : (\nabla\nabla\phi)_{f_i} + \text{HOT} \tag{19}$$

where HOT is higher-order terms. By substituting ϕ_P and ϕ_N in Eq. (15) with Eq. (17) and (18), respectively, the truncation error for linear interpolation from Eqs. (15) can be obtained as [27]

$$e_l = \phi_{f_i} - \underline{\phi_{f_i}} = -\frac{1}{2}f_x(1 - f_x)|\mathbf{d}|^2(\hat{\mathbf{d}}^2 : (\nabla\nabla\phi)_{f_i}) + \text{HOT} \tag{20}$$

$\hat{\mathbf{d}}$ being a unit vector in the direction of $\mathbf{d}$ (Figure 2*b*).

From Eq. (20) it follows that the truncation error for the gradient interpolated using Eq. (16) has the form

$$(\nabla e)_l = (\nabla\phi)_{f_i} - \underline{(\nabla\phi)_{f_i}} = -\frac{1}{2}f_x(1 - f_x)|\mathbf{d}|^2(\hat{\mathbf{d}}^2 : (\nabla\nabla\nabla\phi)_{f_i}) + \text{HOT} \tag{21}$$

Taking the difference between Eq. (19) and Eq. (14), the truncation error for the linear interpolation scheme, which is of second order on every mesh, can be obtained in the following form:

$$\begin{aligned} e_{\text{interpolation}} = &-\frac{1}{2}|\mathbf{d}|^2\left\{f_x(1 - f_x)[\hat{\mathbf{d}}^2 : (\nabla\nabla\phi)_{f_i})] + \psi|\mathbf{d}|\hat{\mathbf{m}} \cdot [\hat{\mathbf{d}}^2 : (\nabla\nabla\nabla\phi)_{f_i}]\right\} \\ &+ \frac{\psi^2}{2}|\mathbf{d}|^2[\hat{\mathbf{m}}^2 : (\nabla\nabla\phi)_{f_i}] + \text{HOT} \end{aligned} \tag{22}$$

Here, $\hat{\mathbf{d}}$ and $\hat{\mathbf{m}}$ and are unit vectors in the directions of $\mathbf{d}$ and $\mathbf{m}$, respectively. This error reduces with the square of the distance between the neighboring nodes and is minimized when the mesh is not skewed ($\psi = 0$) and uniform $f_x = 0.5$. Note that nonorthogonality does not influence the accuracy of the linear interpolation practice. It is well known that the linear interpolation scheme, usually called central differencing (CD), can lead to nonphysical oscillations [27], which are often damped by blending the linear interpolation scheme with the upwind differencing (UD) scheme, which is of first order. The dissipative effects of the UD scheme have been described in many textbooks [27, 28] and will not be treated in this study.

Finally, the error for the convection term is a sum of errors due to interpolation onto the faces weighted by the face flux, thus,

$$e_{\text{conv}} = \sum_f F\, e_{\text{interpolation}} \tag{23}$$

and it depends on the shape of the control volume. Note that mesh-to-flow alignment, present when $F = 0$ at most faces of the control volume, is desirable because such faces do not contribute to the convection transport and therefore do not contribute to the discretization error.

Let us now consider two faces of the control volume in order to show some interesting properties of this discretization practice. By denoting the transport velocities at the faces with $\mathbf{U}_1$ and $\mathbf{U}_2$, respectively, and where $\mathbf{S}_1$ and $\mathbf{S}_2$ are the normal vectors of the respective faces we can write the following:

$$\mathbf{U}_1 - \mathbf{U}_2 = \Delta\mathbf{U} \tag{24}$$

$$\mathbf{S}_1 + \mathbf{S}_2 = \Delta\mathbf{S} \tag{25}$$

The error on two faces can be written:

$$\begin{aligned}
&(\mathbf{U}_1 \cdot \mathbf{S}_1) e_{\text{interpolation1}} + (\mathbf{U}_2 \cdot \mathbf{S}_2) e_{\text{interpolation2}} \\
&\quad = (\mathbf{U}_1 \cdot \mathbf{S}_1) e_{\text{interpolation1}} + [(\mathbf{U}_1 - \Delta\mathbf{U}) \cdot (\Delta\mathbf{S} - \mathbf{S}_1)] e_{\text{interpolation2}} \\
&\quad = (\mathbf{U}_1 \cdot \mathbf{S}_1) e_{\text{interpolation1}} - e_{\text{interpolation2}} \\
&\qquad + (\mathbf{U}_1 \cdot \Delta\mathbf{S} - \Delta\mathbf{U} \cdot \Delta\mathbf{S} + \Delta\mathbf{U} \cdot \mathbf{S}_1) e_{\text{interpolation2}}
\end{aligned} \tag{26}$$

Equation (26) exhibits the following:

1. Face pairs $|\Delta\mathbf{S}| = 0$, faces with the opposite orientation and the same area magnitude, reduce the error because the error on a face is canceled by the error on the other face. The effect of face pairs on the accuracy will be treated in more detail in Section 3.
2. The abrupt changes of the transport velocity $|\Delta\mathbf{U} \cdot \mathbf{S}| \gg 0$ increases the error in the solution because it reduces the effect of error cancellation. This is significant in the case of shocks.
3. The difference in the error of the linear interpolation scheme is dependent on the solution type as shown in Eq. (22). It is desirable that the vectors $\mathbf{d}$ and $\mathbf{m}$ are collinear in the case of smoothly varying solutions. If the second gradient is dominant, it is advisable to keep the mesh as uniform as possible and the vectors $\mathbf{d}$ and $\mathbf{m}$ pointing in the opposite direction and having the same magnitude.

2.2. Diffusion Term

The discrete approximation of the diffusion term is

$$\sum_f \underline{(\Gamma_\phi)_f (\mathbf{S} \cdot \nabla\phi)_f} + e_{\text{diff}} \tag{27}$$

where the terms $\underline{(\Gamma_\phi)_f}$, and $\underline{(\mathbf{S} \cdot \nabla\phi)_f}$ need further treatment. The former is interpolated onto the faces using Eq. (14).

Approximation of $\underline{(\mathbf{S} \cdot \nabla\phi)_f}$ is performed using the following expression [32]:

$$\underline{(\mathbf{S} \cdot \nabla\phi)_f} = |\Delta| \frac{\phi_N - \phi_P}{|\mathbf{d}|} + \mathbf{k} \cdot \underline{(\nabla\phi)_f} + e_{\text{sng}} \tag{28}$$

where $\underline{(\nabla\phi)_f}$ can be evaluated using Eq. (16). Here, Δ is parallel with $\mathbf{d}$, where Δ and $\mathbf{k}$ have the property (Figure 3)

$$\mathbf{S} = \Delta + \mathbf{k} \tag{29}$$

The length of Δ can be expressed as [32]

$$|\Delta| = \frac{|\mathbf{S}|}{\cos \alpha_N} \tag{30}$$

and the length of $\mathbf{k}$ can be calculated from

$$|\mathbf{k}| = |\mathbf{S}| \tan \alpha_N \tag{31}$$

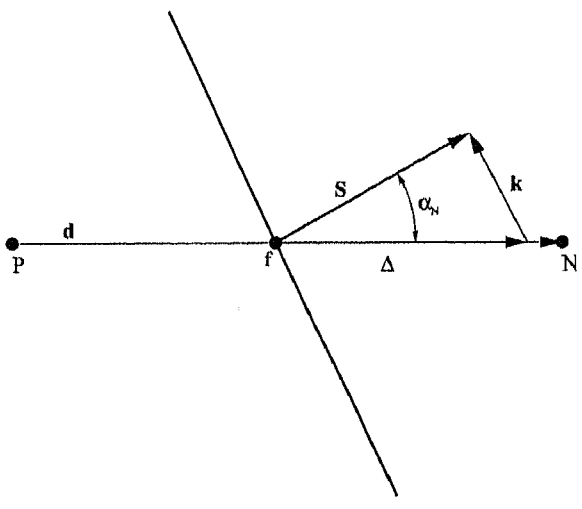

Figure 3. Nonorthogonality treatment.

The truncation error e_{sng} for the approximation of the $(\mathbf{S}\cdot\nabla\phi)_f$ term can be obtained using the following Taylor expansions:

$$\phi_P = \phi_f + (\mathbf{x}_P - \mathbf{x}_f)\cdot(\nabla\phi)_f + \frac{1}{2}(\mathbf{x}_P - \mathbf{x}_f)^2 : (\nabla\nabla\phi)_f + \frac{1}{6}(\mathbf{x}_P - \mathbf{x}_f)^3 :: (\nabla\nabla\nabla\phi)_f + \text{HOT} \tag{32}$$

$$\phi_N = \phi_f + (\mathbf{x}_N - \mathbf{x}_f)\cdot(\nabla\phi)_f + \frac{1}{2}(\mathbf{x}_N - \mathbf{x}_f)^2 : (\nabla\nabla\phi)_f + \frac{1}{6}(\mathbf{x}_N - \mathbf{x}_f)^3 :: (\nabla\nabla\nabla\phi)_f + \text{HOT} \tag{33}$$

By substituting Eq. (32) and Eq. (33) into Eq. (28) and adding the error from the interpolation of $\underline{(\nabla\phi)_f}$, the truncation error for $(\mathbf{S}\cdot\nabla\phi)_f$ is obtained:

$$\begin{aligned} e_{\text{sng}} &= (\mathbf{S}\cdot\nabla\phi)_f - \underline{(\mathbf{S}\cdot\nabla\phi)_f} \\ &= -\frac{|\mathbf{S}|}{\cos\alpha_N}\frac{|\mathbf{d}|}{2}(2f_x - 1)\hat{\mathbf{d}}^2 : (\nabla\nabla\phi)_f \\ &\quad - \frac{|\mathbf{S}|}{6\cos\alpha_N}|\mathbf{d}|^2[(1-f_x)^3 + f_x^3]\hat{\mathbf{d}}^3 :: (\nabla\nabla\nabla\phi)_f \\ &\quad - |\mathbf{S}|\tan\alpha_N\frac{|\mathbf{d}|^2}{2}f_x(1-f_x)\hat{\mathbf{k}}\cdot[\hat{\mathbf{d}}^2 : (\nabla\nabla\nabla\phi)_f] + \text{HOT} \end{aligned} \tag{34}$$

where $\hat{\mathbf{d}}$ and $\hat{\mathbf{k}}$ are unit vectors in directions $\mathbf{d}$ and $\mathbf{k}$, respectively, and f_x is the linear interpolation factor defined in Eq. (12). From the dependence of Eq. (34) on f_x, it follows that the approximation is of first order except for $f_x = 0.5$, i.e., when the mesh is uniform and the approximation is of second order. The error is also dependent on the angle of nonorthogonality and is minimal when $\alpha_N = 0$. Note that mesh skewness does not influence the accuracy of the diffusion term discretization.

The truncation error for the diffusion term is the sum of errors on the faces, and has the form

$$\begin{aligned} e_{\text{diff}} &= \sum_f \underline{(\Gamma_\phi)_f}\, e_{sng} + \sum_f e_{\text{interpolation}}\left[|\Delta|\frac{\phi_N - \phi_P}{|\mathbf{d}|} + \mathbf{k}\cdot\underline{(\nabla\phi)_f}\right] \\ &\quad + \sum_f e_{\text{interpolation}}\, e_{\text{sng}} \end{aligned} \tag{35}$$

from which it follows that the order of the approximation is equal to the lowest order found in Eqs. (34) and (22). This error depends on the shape of the control volume. The overall error is dependent on the error of the linear interpolation scheme in the case of variable diffusion coefficient, and on the error from the approximation of the surface-normal gradient. By taking two arbitrary faces of the control volume and analyzing their contribution to the error, as in the case of the convection term, it can be noticed that the errors cancel each other if the vectors $\mathbf{d}$ and $\mathbf{k}$ are collinear and point in opposite directions, present in the case when the faces form a pair. This will be treated in more detail in Section 3.

2.3. Source Term

The discrete form of the source term is

$$\int_{V_P} S_\phi(\phi)\, dV = Su\ V_P + Sp\ V_P\ \phi_P + e_{\text{source}} \tag{36}$$

The truncation error for the source term can be estimated by using the following Taylor expansion:

$$\begin{aligned}\int_{V_P} S(\mathbf{x},\phi)dV = &\int_{V_P}\left\{S(\mathbf{x}_P,\phi_P) + (\mathbf{x}-\mathbf{x}_P)\cdot[\nabla S(\mathbf{x},\phi)]_P + \Delta\phi\frac{\partial S(\mathbf{x},\phi)}{\partial\phi}\right\}dV\\ &+\int_{V_P}\left\{\frac{1}{2}(\mathbf{x}-\mathbf{x}_P)^2 :: [\nabla\nabla S(\mathbf{x},\phi)]_P\right\}dV\\ &+\int_{V_P}\left\{\frac{1}{2}(\mathbf{x}-\mathbf{x}_P)\cdot[\nabla S(\mathbf{x},\phi)]_P\Delta\phi\frac{\partial S}{\partial\phi}\right\}dV\\ &+\int_{V_P}\left(\frac{1}{2}(\Delta\phi)^2\frac{\partial^2 S(\mathbf{x},\phi)}{\partial\phi^2}\right)dV\end{aligned} \tag{37}$$

where $\Delta\phi$ stands for

$$\Delta\phi = (\mathbf{x}-\mathbf{x}_P)\cdot(\nabla\phi)_P \tag{38}$$

After substituting $\Delta\phi$ and $S(\mathbf{x}_P,\phi_P) + \Delta\phi[\partial S(\mathbf{x},\phi)/\partial\phi]$ in Eq. (37) with Eq. (38), the truncation error can be found as the difference between Eq. (37) and Eq. (36):

$$\begin{aligned}e_{\text{source}} = &\frac{1}{2}(\mathbf{x}-\mathbf{x}_P)^2 : (\nabla\nabla S)_P\ V_P + \frac{1}{2}(\mathbf{x}-\mathbf{x}_P)^2 : [(\nabla\phi)_P(\nabla S)_P]\frac{\partial S}{\partial\phi}V_P\\ &+\frac{1}{2}(\mathbf{x}-\mathbf{x}_P)^2 : [(\nabla\phi)_P]^2\frac{\partial^2 S(\mathbf{x},\phi)}{\partial\phi^2}V_P\end{aligned} \tag{39}$$

The error is not a sum of face errors and it is therefore not critically dependent on the shape of the control volume, but on its size.

3. TRUNCATION ERRORS FOR CONVECTION AND DIFFUSION TERMS FOR DIFFERENT SHAPES OF CONTROL VOLUMES

The aim of this section is to determine the influence of various cell types on the discretization error. In order to simplify the analysis, the effects of nonorthogonality, skewness, and nonuniformity will not be considered because they are not the properties of the studied cell types, but the artefacts a low-quality mesh. The analysis will be performed on 2-D cell types in order to reduce the number of terms in the equations, due to the smaller number of faces than in their 3-D counterparts, but it still remains valid for 3-D cell types.

The shapes of control volumes used for this analysis are squares, triangles, and hexagons. Triangles are chosen because they are the simplest shape without face

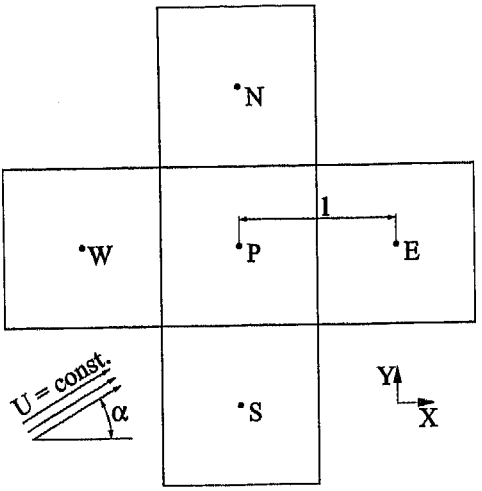

Figure 4. Square mesh.

pairs, squares are the shape with the smallest number of face pairs, and hexagons are chosen to find out how the increased number of face pair affects the accuracy. The properties of such meshes are as follows.

1. **Square mesh.** A representative cell with its neighbors which influence it are shown in Figure 4. This mesh is orthogonal, it is not skewed, and uniform $f_x = 0.5$ because the center of each internal face lies midway between the neighboring nodes.
2. **Triangular mesh.** A mesh consisting of equilateral triangles is uniform $f_x = 0.5$, orthogonal, and not skewed; see Figure 5.
3. **Regular hexagonal mesh.** This type of mesh can be generated using a Delaunay algorithm [36]. It consists of hexagons and is uniform, orthogonal, and not skewed, see Figure 6.

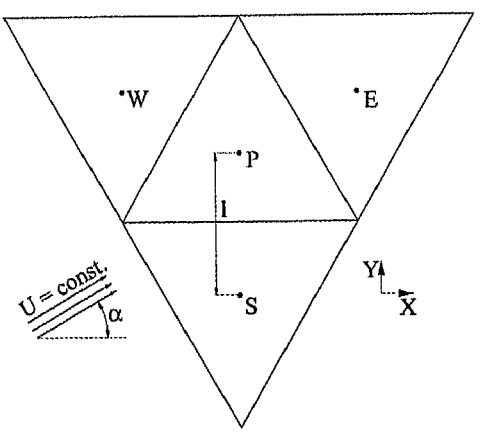

Figure 5. Triangular mesh.

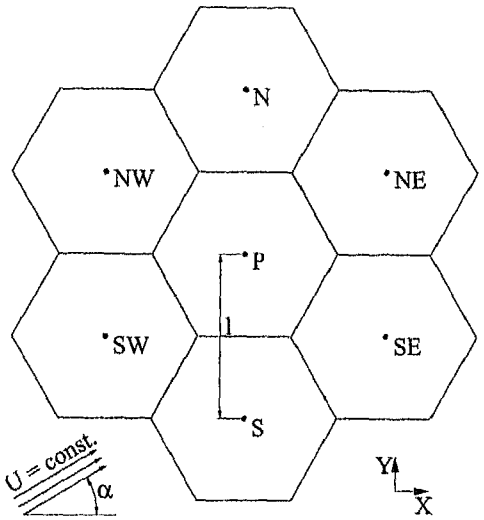

Figure 6. Hexagonal mesh.

3.1. Convection Term

The analysis of errors in the convection term will be performed by using the linear interpolation scheme and taking the fluid velocity to be constant:

$$\mathrm{U} = \text{const.}$$

1. **Error analysis for a square mesh.** The distance between the two nodes is equal to the length of a side. Hence, the mass flux is

$$F = \rho|\mathbf{U}|l \tag{40}$$

because $|\mathbf{S}| = l$; and $f_x = 0.5$. Replacing $|\mathbf{d}|$ in Eq. (22) with l yields

$$\begin{aligned} e_{\text{convSquare}} &= -\frac{1}{8}F\cos\alpha\, l^2(\mathbf{n}_e^2 : (\nabla\nabla\phi)_e) - \frac{1}{8}F\sin\alpha\, l^2(\mathbf{n}_n^2 : (\nabla\nabla\phi)_n) \\ &\quad + \frac{1}{8}F\cos\alpha\, l^2(\mathbf{n}_w^2 : (\nabla\nabla\phi)_w) + \frac{1}{8}F\sin\alpha\, l^2(\mathbf{n}_s^2 : (\nabla\nabla\phi)_s) \\ &= -\frac{1}{8}\, l^2F\cos\alpha(\mathbf{n}_e^2 : ((\nabla\nabla\phi)_e - (\nabla\nabla\phi)_w)) \\ &\quad -\frac{1}{8}\, l^2F\sin\alpha(\mathbf{n}_n^2 : ((\nabla\nabla\phi)_n - (\nabla\nabla\phi)_s)) \end{aligned} \tag{41}$$

where $\hat{\mathbf{d}}$ from Eq. (22) is replaced by $\mathbf{n}$, which represents a unit-face-normal vector pointing outwards from the cell P. The subscript $\mathbf{n}_e$ denotes that the face is shared with a neighbor E. α is the angle between the velocity vector and the x axis.

2. **Equilateral triangular mesh.** For this mesh the mass flux is

$$F = \sqrt{3}\rho|\mathbf{U}|l \tag{42}$$

The truncation error can be found using Eq. (22), yielding

$$e_{\text{convTri}} = -\frac{\sqrt{3}}{16} l^2 F \cos\alpha \{[\mathbf{n}_e^2 : (\nabla\nabla\phi)_e] - [\mathbf{n}_w^2 : (\nabla\nabla\phi)_w]\}$$
$$-\frac{1}{8} l^2 F \sin\alpha \left\{\frac{1}{2}[\mathbf{n}_e^2 : (\nabla\nabla\phi)_e] - [\mathbf{n}_s^2 : (\nabla\nabla\phi)_s] - \frac{1}{2}[\mathbf{n}_w^2 : (\nabla\nabla\phi)_w]\right\} \quad (43)$$

3. **Hexagonal mesh.** Here the expression for the mass flux is

$$F = \frac{\sqrt{3}}{3} \rho |\mathbf{U}| l \quad (44)$$

and Eq. (22) gives the truncation error as

$$e_{\text{convHexagon}} = -\frac{\sqrt{3}}{16} l^2 F \cos\alpha \{\mathbf{n}_{ne}^2 : [(\nabla\nabla\phi)_{ne} - (\nabla\nabla\phi)_{sw}]\}$$
$$-\frac{\sqrt{3}}{16} l^2 F \cos\alpha \{\mathbf{n}_{se}^2 : [(\nabla\nabla\phi)_{se} - (\nabla\nabla\phi)_{nw}]\}$$
$$-\frac{1}{8} l^2 F \sin\alpha [\mathbf{n}_n^2 : ((\nabla\nabla\phi)_n - (\nabla\nabla\phi)_s)]$$
$$-\frac{1}{16} l^2 F \sin\alpha \{\mathbf{n}_{ne}^2 : [(\nabla\nabla\phi)_{ne} - (\nabla\nabla\phi)_{sw}]\}$$
$$-\frac{1}{16} l^2 F \sin\alpha \{\mathbf{n}_{se}^2 : [(\nabla\nabla\phi)_{se} - (\nabla\nabla\phi)_{nw}]\} \quad (45)$$

Evidently, the error in Eqs. (41), (43), and (45) is dependent on both the spatial resolution and the form of the solution itself, as expressed through its gradients. A comparison of accuracy can therefore only be performed by examining different forms of solutions, as follows.

1. $\nabla\phi = \text{constant}$. When the solution field has a uniform and fixed gradient, the error is zero on all types of meshes. This is consistent with the assumption expressed in Eq. (4).
2. $\nabla\nabla\phi = \text{constant}$. This class of solutions with uniform curvature reveals differences in accuracy between different mesh types. The discretization on square and hexagonal meshes still produces exact solutions Eqs. (41) and (45), while on triangular meshes it produces errors. The truncation error for triangular meshes, Eq. (43), can be simplified to

$$e_{\text{convTri}} = -\frac{\sqrt{3}}{16} l^2 F \cos\alpha [(\mathbf{n}_e^2 - \mathbf{n}_w^2) : \nabla\nabla\phi]$$
$$-\frac{1}{8} l^2 F \sin\alpha \left[\left(\frac{1}{2}\mathbf{n}_e^2 - \mathbf{n}_s^2 - \frac{1}{2}\mathbf{n}_w^2\right) : \nabla\nabla\phi\right] \quad (46)$$

The above equation shows that the errors exist because triangles do not have face pairs, such that the error on each pair cancels out. Two cell faces form a face pair if the sum of their outward-pointing normal vectors is a zero vector. It follows that the difference between the diadic tensors of the face normals, i.e., $(\mathbf{n}_e^2 - \mathbf{n}_w^2) = \mathbf{0}$, is a zero tensor for every face pair; which results in zero discretization error for squares and hexagons. Triangular meshes do not have any face pairs because $(\mathbf{n}_e^2 - \mathbf{n}_w^2)$ and $\left(\frac{1}{2}\mathbf{n}_e^2 - \mathbf{n}_s^2 - \frac{1}{2}\mathbf{n}_w^2\right)$ in Eq. (46) are not zero tensors.

3. $\nabla\nabla\nabla\phi = \text{constant}$. This type of problem cannot be resolved exactly on any type of mesh. Hence, it should show which of the square or hexagon shapes should be more accurate. The variation of $\nabla\nabla\phi(\mathrm{x})$ within the cell is

$$\nabla\nabla\phi(\mathbf{x}) = (\nabla\nabla\phi)_{\mathrm{P}} + (\mathbf{x} - \mathbf{x}_P) \cdot \nabla\nabla\nabla\phi \tag{47}$$

When $\nabla\nabla\phi$ in Eq. (22) is substituted with Eq. (47), the following expressions for the truncation errors result:

$$e_{\text{convSquare}} = -\frac{1}{8} l^3 F \cos\alpha\, \mathbf{n}_e^3 :: \nabla\nabla\nabla\phi - \frac{1}{8} l^3 F \sin\alpha\, \mathbf{n}_n^3 :: \nabla\nabla\nabla\phi \tag{48}$$

$$\begin{aligned} e_{\text{convHexagon}} = &-\frac{1}{8} l^3 F \cos\alpha \frac{\sqrt{3}}{2}\left(\mathbf{n}_{ne}^3 + \mathbf{n}_{nw}^3\right) :: \nabla\nabla\nabla\phi \\ &-\frac{1}{8} l^3 F \sin\alpha\left(\mathbf{n}_n^3 + \frac{1}{2}\mathbf{n}_{ne}^3 - \frac{1}{2}\mathbf{n}_{nw}^3\right) :: \nabla\nabla\nabla\phi \end{aligned} \tag{49}$$

In order to get an idea which type of mesh is more accurate, the problem is simplified such that $\partial^3\phi/\partial x^3 = \text{constant}$, while all other components of $\nabla\nabla\nabla\phi$ are zero. The velocity $\mathbf{U}$ is at the angle of $\alpha = 0$. When the above is inserted in Eqs. (48) and (49), there results

$$e_{\text{convSquare}} = -\frac{1}{8} l^3 F \frac{\partial^3\phi}{\partial x^3} \tag{50}$$

$$e_{\text{convHexagon}} = -\frac{9}{64} l^3 F \frac{\partial^3\phi}{\partial x^3} \tag{51}$$

For the same number of cells in the domain, the area of the square cell is equal to the area of the hexagon. From there it follows that

$$l_{\text{hexagon}} = -\frac{2\sqrt{3}}{3} l_{\text{square}} \tag{52}$$

By knowing the ratio between l_{hexagon} and l_{square}, Eq. (52), the ratio between the errors is

$$\frac{e_{\text{convHexagon}}}{e_{\text{convSquare}}} = 1.155 \tag{53}$$

Equation (53) shows that the error on the hexagonal mesh is expected to be slightly higher than that for the square mesh. The hexagon always has more faces with nonzero mass fluxes than the square, such that the sum of errors on those faces is larger than for the square.

3.2. Diffusion Term

Accuracy of the diffusion term discretization on different mesh types can be performed by comparing the truncation errors defined in Eq. (35). In order to simplify the analysis, the diffusion coefficient Γ_ϕ is assumed to be constant, i.e.,

$$\Gamma_\phi = \text{constant}$$

This makes the error arising from interpolation of Γ_ϕ onto the cell faces equal to zero; and the only remaining error in Eq. (28) comes from the approximation of surface-normal gradients. This will now be evaluated for different mesh types:

1. **Square mesh.** For the configuration depicted in Figure 4, the magnitude of the surface vector is

$$|\mathbf{S}| = l \tag{54}$$

Noting that $|\mathbf{d}| = l$, $\alpha_N = 0$, and $f_x = 0.5$, the truncation error can be written:

$$\begin{aligned} e_{\text{diffSquare}} &= -\frac{1}{24}(\rho\Gamma)|\mathbf{S}|l^2[\mathbf{n}_e^3 :: (\nabla\nabla\nabla\phi)_e] - \frac{1}{24}(\rho\Gamma)|\mathbf{S}|l^2[\mathbf{n}_w^3 :: (\nabla\nabla\nabla\phi)_w] \\ &\quad -\frac{1}{24}(\rho\Gamma)|\mathbf{S}|l^2[\mathbf{n}_n^3 :: (\nabla\nabla\nabla\phi)_n] - \frac{1}{24}(\rho\Gamma)|\mathbf{S}|l^2[\mathbf{n}_s^3 :: (\nabla\nabla\nabla\phi)_s] \\ &= -\frac{1}{24}(\rho\Gamma)|\mathbf{S}|l^2\{\mathbf{n}_e^3 :: [(\nabla\nabla\nabla\phi)_e - (\nabla\nabla\nabla\phi)_w]\} \\ &\quad -\frac{1}{24}(\rho\Gamma)|\mathbf{S}|l^2[\mathbf{n}_n^3 :: ((\nabla\nabla\nabla\phi)_n - (\nabla\nabla\nabla\phi)_s)] \end{aligned} \tag{55}$$

2. Equilateral triangular mesh. The truncation error for this cell type is

$$e_{\text{diffTri}} = -\frac{1}{24}\rho\Gamma|\mathbf{S}|l^2[\mathbf{n}_e^3 :: (\nabla\nabla\nabla\phi)_e + \mathbf{n}_w^3 :: (\nabla\nabla\nabla\phi)_w + \mathbf{n}_s^3 :: (\nabla\nabla\nabla\phi)_s] \tag{56}$$

where $|\mathbf{S}| = \sqrt{3}l$.

3. Equilateral hexagonal mesh

$$\begin{aligned} e_{\text{diffHexagon}} &= -\frac{1}{24}\rho\Gamma|\mathbf{S}|l^2\{\mathbf{n}_n^3 :: [(\nabla\nabla\nabla\phi)_n - (\nabla\nabla\nabla\phi)_s]\} \\ &\quad -\frac{1}{24}\rho\Gamma|\mathbf{S}|l^2\{\mathbf{n}_{ne}^3 :: [(\nabla\nabla\nabla\phi)_{ne} - (\nabla\nabla\nabla\phi)_{sw}]\} \\ &\quad -\frac{1}{24}\rho\Gamma|\mathbf{S}|l^2\{\mathbf{n}_{nw}^3 :: [(\nabla\nabla\nabla\phi)_{nw} - (\nabla\nabla\nabla\phi)_{se}]\} \end{aligned} \tag{57}$$

where $|\mathbf{S}| = (\sqrt{3}/3)l$.

Again, the comparison will be made for different forms of solution fields.

1. $\nabla\nabla\phi = \text{constant}$. Equations (55)–(57) show that the error is zero for all mesh types.
2. $\nabla\nabla\nabla\phi = \text{constant}$. For such fields, exact solutions are produced on meshes consisting of squares, Eq. (55), and hexagons, Eq. (57). The truncation errors for the triangular mesh is

$$e_{\text{diffTri}} = -\frac{1}{24}\rho\Gamma|\mathbf{S}|l^2[(\mathbf{n}_e^3 + \mathbf{n}_w^3 + \mathbf{n}_s^3) :: (\nabla\nabla\nabla\phi)] \tag{58}$$

The error is a consequence of the fact that triangles have an odd number of faces, which are not paired; thus the error on them cannot cancel out. For example, the third-rank tensor $(\mathbf{n}_e^3 + \mathbf{n}_w^3 + \mathbf{n}_s^3)$ in Eq. (58) is not a zero tensor. On the contrary, cell face pairs make the sum of those tensors equal to zero, i.e., $(\mathbf{n}_n^3 + \mathbf{n}_s^3) = \mathbf{0}$ in Eqs. (55) and (57).
3. $\nabla\nabla\nabla\nabla\phi = \text{constant}$. Exact solutions for this type of problem cannot be obtained on any mesh type. The variation of $\nabla\nabla\nabla\phi(\mathrm{x})$ within the domain is

$$\nabla\nabla\nabla\phi(\mathrm{x}) = (\nabla\nabla\nabla\phi)_P + (\mathrm{x} - \mathrm{x}_P)\cdot\nabla\nabla\nabla\nabla\phi \tag{59}$$

The error for the square cell reads

$$e_{\text{diffSquare}} = -\frac{1}{24}\rho\Gamma|\mathbf{S}|l^3(\mathbf{n}_e^4 + \mathbf{n}_n^4) ::: \nabla\nabla\nabla\nabla\phi \tag{60}$$

and the error for hexagon can be written as

$$e_{\text{diffHexagon}} = -\frac{1}{24}\rho\Gamma|\mathbf{S}|l^3(\mathbf{n}_{ne}^4 + \mathbf{n}_n^4 + \mathbf{n}_{nw}^4) ::: \nabla\nabla\nabla\nabla\phi \tag{61}$$

In order to get an insight into the error behavior on such problems, the problem is simplified to $\partial^4\phi/\partial x^4 = \textit{constant}$ while all other components of are zero. By inserting this into Eqs. (60) and (61), there results

$$e_{\text{diffSquare}} = -\frac{1}{24}(\rho\Gamma)|\mathbf{S}|l^3\frac{\partial^4\phi}{\partial x^4} \tag{62}$$

$$e_{\text{diffHexagon}} = -\frac{1}{24}(\rho\Gamma)l^3\frac{9}{8}\frac{\partial^4\phi}{\partial x^4} \tag{63}$$

By comparing Eqs. (62) and (63) on meshes with the same number of cells, there results

$$\frac{e_{\text{diffHexagon}}}{e_{\text{diffSquare}}} = 1.155 \tag{64}$$

These results are valid for 3-D cell types; a tetrahedron is the cell type with the smallest number of faces without any face pairs, and it corresponds to a triangle in two dimensions. The approximation of the convection term is exact only for solutions with constant gradient, and the diffusion term discretization is exact for solutions with constant curvature. A hexahedron has the smallest number of face pairs in three

dimensions and corresponds to a square in this analysis. The approximation of the convection term on the hexahedron is exact for solutions with constant curvature, and the discretization of the diffusion term is exact for solutions with the constant third gradient.

4. NUMERICAL EXAMPLES

In order to validate the above analysis, two laminar-flow cases will be used. Testing will be performed on meshes consisting of quadrilaterals, triangles, and polygons. Polygonal meshes consist mainly of hexagons studied in the previous section. The discretization error will be measured as the difference between the calculated value and the exact value at the cell centers, and given as its absolute value. The discretization error is a consequence of the inexact discretization practice, measured by the studied truncation errors, and therefore it is proportional to the intensity of truncation errors within the domain. Reduction of the maximum and mean error on meshes with the increased number of cells, generated by halving the mean edge length, will be monitored in order to establish relations between the solution quality on different mesh types. Each mesh will be generated by the mesh generator by halving the specified mean edge length of the previous one. The mean error is calculated using

$$e_{\text{mean}} = \frac{\sum_{i=0}^{n} |e_i| V_i}{\sum_{i=0}^{n} V_i} \tag{65}$$

where $|e_i|$ is the error at the cell center and V_i is the volume of the current cell.

4.1. Planar Jet

In this test case, a fluid enters a planar 2-D domain via a slot, see Figure 7, forming a jet.

The analytical solution for the U_x velocity component, which can be found in [50], was derived by assuming the flow is incompressible with uniform pressure and a small cross-stream velocity:

$$\mathbf{U}_x = \left(\frac{3}{200}\mathrm{Re}\right)^{1/3} X^{-1/3} \operatorname{sech}^2\left[\left(\frac{\mathrm{Re}^2}{1875}\right)^{1/3} Y\, X^{-2/3}\right] \tag{66}$$

The expression for the cross-stream component is obtained from the continuity equation:

$$\begin{aligned}\mathbf{U}_y = &-\frac{1}{3}\left(\frac{225}{8}\frac{1}{\mathrm{Re}}\right)^{1/3} X^{-2/3} \tanh\left[\left(\frac{\mathrm{Re}^2}{1875}\right)^{1/3} Y\, X^{-2/3}\right] \\ &+\frac{2}{3}\left(\frac{3}{200}\mathrm{Re}\right)^{1/3} Y\, X^{-4/3} \operatorname{sech}^2\left[\left(\frac{\mathrm{Re}^2}{1875}\right)^{1/3} Y\, X^{-2/3}\right]\end{aligned} \tag{67}$$

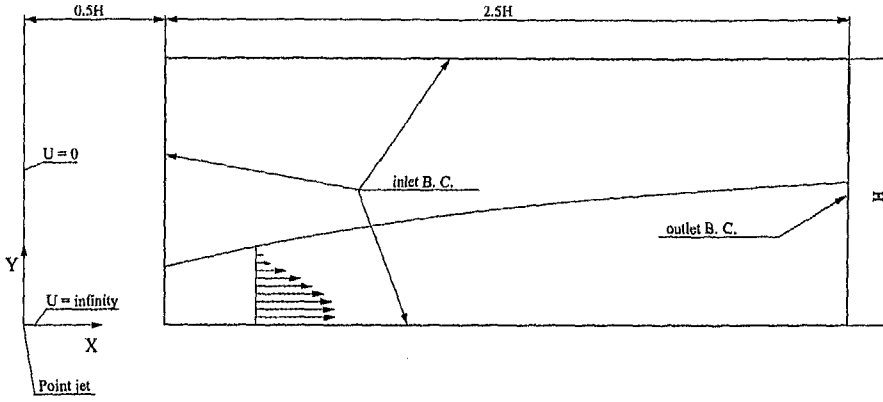

Figure 7. Geometry and boundary conditions for the planar jet.

Note that Eqs. (66) and (67) represent the approximate solution of the Navier-Stokes system, which limits their usability to solutions on coarse meshes where the discretization error is considerably larger than the error in the above approximation.

The current example is at Re = 520, which is based on the maximum velocity, found in the lower-left corner of the domain, and the domain length.

The solution was sought on five meshes for every cell type. Their sizes and quality measures are given in Table 1. Each mesh was generated by the mesh generator, and the meshes with the same number have the same average edge length. The refinement was performed by halving the specified edge length to the mesh generator. The values of average skewness, average uniformity, and average nonorthogonality show that the mesh quality is very close to the theoretical situation studied in the previous section and therefore the influence of skewness, nonuniformity, and nonorthogonality is not considered important. All calculations were performed by using the linear

Table 1. Number of cells and mesh quality measures for different types of meshes (jet case)

Mesh type	No.	No. of cells	Average ψ	Average f_x	Average α_N deg
Quadrilaterals	1	18	0.0	0.5	0.0
	2	72	0.0	0.5	0.0
	3	288	0.0	0.5	0.0
	4	1,152	0.0	0.5	0.0
	5	4,608	0.0	0.5	0.0
Polygons	1	19	0.052	0.402	6.71
	2	59	0.059	0.439	4.97
	3	211	0.037	0.472	3.72
	4	782	0.021	0.484	2.85
	5	3,063	0.011	0.493	2.79
Triangles	1	20	0.057	0.443	16.0
	2	86	0.037	0.467	11.0
	3	362	0.026	0.484	7.10
	4	1,448	0.012	0.491	5.14
	5	5,898	0.008	0.496	3.73

interpolation scheme for the convection term, and the boundary conditions were set according to Figure 7. Boundary conditions are set consistently for all meshes by assigning the values of the velocity at the face centers at inlet boundaries and by setting the normal gradient to zero at outlet boundaries. The pressure is set to zero at the outlet boundary, and the normal gradient is set to zero at inlet boundaries. Hence, the boundary conditions do not cause differences in accuracy on different mesh types.

The meshes corresponding to the number 3 in the Table 1 are shown in Figures 8*a*, 8*b*, and 8*c*. Figure 8*b* shows that most cells in the polygonal mesh are hexagons.

Figure 9*a* shows that for the same number of cells, the maximum exact error is largest on triangular meshes, while it is at the same level for polygonal and quadrilateral meshes when the mesh becomes fine. The mean error depicted in Figure 9*b* also behaves according to the findings from the previous section. The mean error is lowest on quadrilateral meshes and largest on the triangular ones. On fine meshes, all mesh types tend to the same curve, which is the influence of the approximations used for deriving the analytical solution.

4.2. Flow over a Cavity

The second case considered is a 2-D incompressible laminar channel flow with a cavity in the bottom wall; see Figure 10.

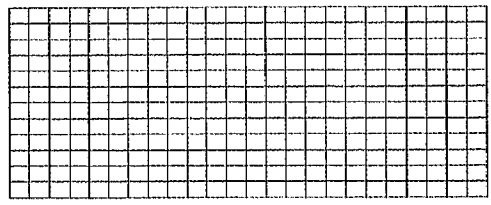

(*a*) Quadrilateral mesh (288 cells)

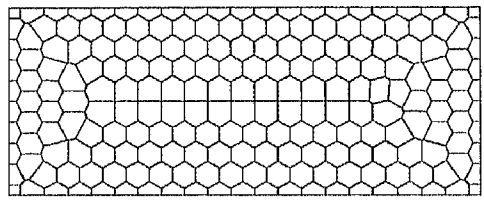

(*b*) Polygonal mesh (211 cells)

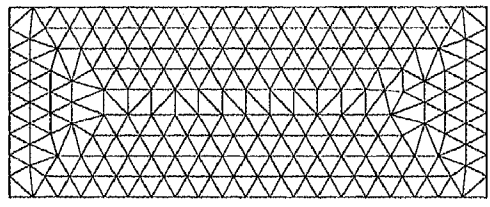

(*c*) Triangular mesh (362 cells)

Figure 8. Meshes for the jet case.

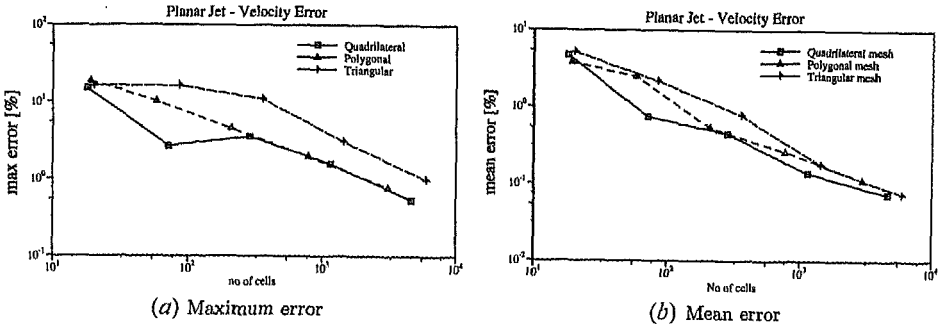

(*a*) Maximum error (*b*) Mean error

Figure 9. Variation of errors for the jet case. Errors are given as percentage of the maximum velocity found at (0.5H, 0).

The flow is at Re = 200 based on the channel height H and the average inlet velocity U_{avg}. At the inlet, a parabolic velocity profile is prescribed. Boundary conditions are prescribed consistently for all meshes and therefore they should not affect the accuracy of different mesh types. Additionally, the flow in the channel is a flow with constant curvature, which will be resolved exactly on the quadrilateral and polygonal meshes, and the triangular meshes produce errors there. Therefore, the accuracy on the triangular meshes is expected to be significantly worse than on the other ones. However, this problem has no analytical solution, so the benchmark solution, considered error-free, was obtained on a fine mesh with approximately 500,000 cells. The maximum error in the benchmark solution is estimated to 0.57% of the average inlet velocity using the Richardson extrapolation [27], and the average error in the benchmark solution is estimated to 0.002%.

Four meshes of each type, summarized in Table 2, were used to determine which type gives the best accuracy, and to monitor the reduction of error on a set of meshes of each type generated by halving the specified average edge length. The convergence of the predicted pressure-drop coefficient was also monitored. The quality of the meshes is high, and the effects of skewness, nonuniformity, and nonorthogonality are not considered important. The calculations were performed using the linear interpolation scheme for the convection term.

The quadrilateral, polygonal, and triangular meshes corresponding to the number 2 in Table 2 are shown in Figures 11*a*, 11*b*, and 11*c*.

Variations of maximum and mean errors in the velocity field for different types of meshes are given in Figures 12*a* and 12*b*, respectively. Triangular meshes have the

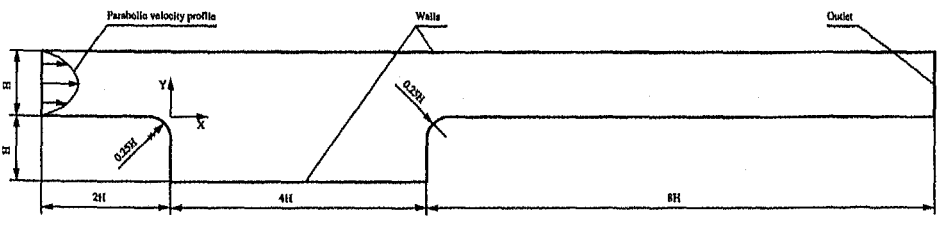

Figure 10. Geometry and boundary conditions for the flow over a cavity.

Table 2. Number of cells and mesh quality measures for different types of meshes (cavity case)

Mesh type	No.	No. of cells	Average ψ	Average f_x	Average α_N deg
Quadrilaterals	1	594	0.005	0.494	4.54
	2	2,376	0.002	0.497	4.69
	3	9,504	0.001	0.498	4.77
	4	38,016	0.0006	0.499	4.8
Polygons	1	556	0.042	0.464	4.33
	2	2,159	0.022	0.483	2.98
	3	8,487	0.012	0.492	2.00
	4	33,352	0.006	0.495	1.51
Triangles	1	950	0.025	0.478	9.53
	2	3,996	0.011	0.489	6.39
	3	16,336	0.007	0.495	4.70
	4	65,430	0.003	0.497	3.31

largest error for the same number of cells, as expected. The maximum errors found on quadrilateral meshes are almost the same as on the polygonal meshes, which is in agreement with the analysis presented in the previous section. The unexpected behavior of the maximum error on the quadrilateral mesh between the first and second cycles is attributed to inadequate resolution in the critical regions; see Figure 11*a*. Triangular meshes have the largest average exact error for a given number of cells and require almost 10 times more cells to achieve the same accuracy as on the quadrilateral meshes. The average error on polygonal meshes is much closer to the quadrilateral mesh result, requiring approximately twice as many cells to achieve the same accuracy. The reduction of the average exact error is very close

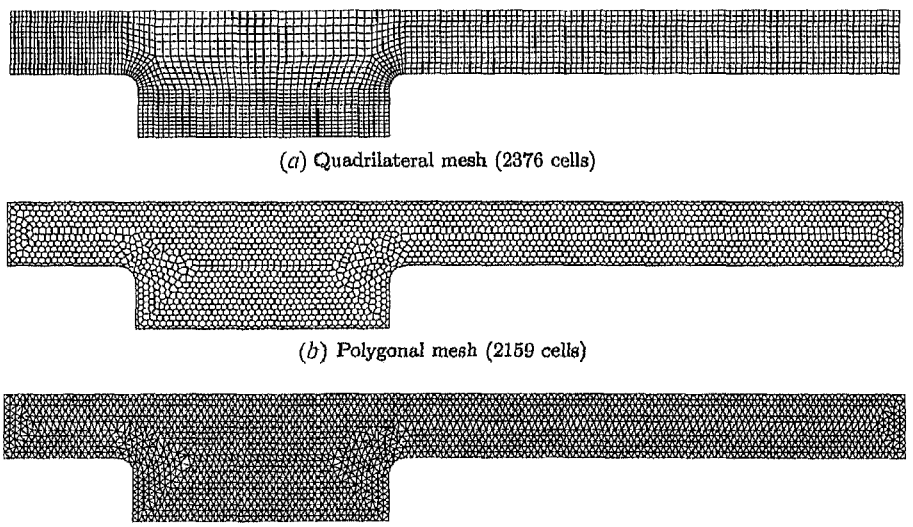

(*a*) Quadrilateral mesh (2376 cells)

(*b*) Polygonal mesh (2159 cells)

(*c*) Triangular mesh (3996 cells)

Figure 11. Meshes for the cavity case.

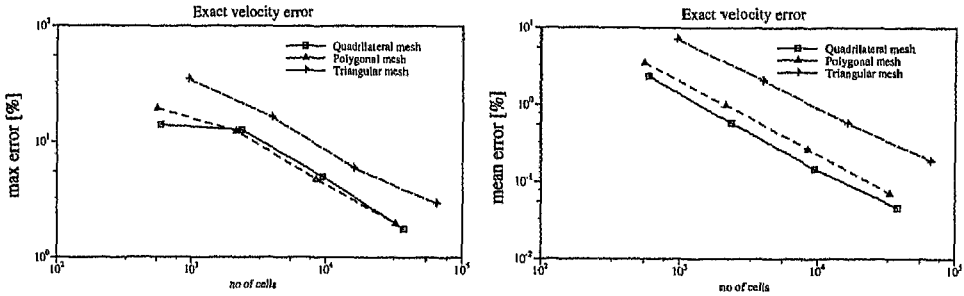

(*a*) Maximum error (*b*) Mean error

Figure 12. Variation of errors for the cavity case. Errors are given as percentage of average inlet velocity U_{avg}.

Table 3. Scaling of C_p for different types of meshes (cavity case)

Pressure-drop coefficient (C_p)					
Quadrilateral		Polygonal		Triangular	
Cells	C_p	Cells	C_p	Cells	C_p
594	1.43128	556	1.59121	950	1.96345
2,376	1.49723	2,159	1.53935	3,996	1.67216
9,504	1.51544	8,487	1.52665	16,336	1.56432
38,016	1.51982	33,352	1.52333	65,430	1.53555
Mesh-independent value $C_p = 1.5203$					

to the theoretical second-order reduction rate for all types of meshes, and it deteriorates when the mesh becomes fine. This is caused by the remaining error in the benchmark solution, as its influence is larger on fine meshes.

A comparison of the pressure-drop coefficients (C_p) given in Table 3 shows that on the quadrilateral and polygonal meshes C_p tends to the mesh-independent value faster than on its triangular counterpart. The magnitude of the error is almost the same for quadrilateral and polygonal meshes for all mesh sizes, and much smaller than the error on triangular meshes.

5. SUMMARY AND FUTURE WORK

This article presented an analysis of truncation errors for a second-order finite-volume method on square, triangular, and hexagonal meshes because they completely fill a 2-D space. The analysis has shown that squares are the most accurate type of cells in two dimensions because of face pairs which cancel the error and the smallest possible number of face pairs. It was shown why the triangular meshes are the least accurate type of meshes; because triangles do not have face pairs. The analysis reveals that errors on hexagonal meshes are expected to be slightly larger than on square meshes because they have more faces contributing to the transport of the given property. However, the merit of using hexagonal meshes is in the fact

that their generation can be made automatic much more easily than for quadrilateral meshes. This results also apply for a 3-D case, where hexahedral meshes are expected to be the most accurate because they have the smallest possible number of face pairs, while tetrahedral meshes are expected to be the least accurate type of mesh because the tetrahedra do not have face pairs which would cancel the error out. The above results were tested on two laminar-flow examples, which corroborate the analysis.

It was also shown that skewness has an adverse effect on the accuracy of interpolation on the face, nonorthogonality increases the error of the approximation of the surface-normal gradient, and nonuniformity reduces the order of the approximation of the surface-normal gradient to firstorder. The detailed analysis of their effect on accuracy is not within the scope of this work because of the vast number of possible cases appearing in practice. Future work could consist of studying the effect of nonorthogonality, skewness, nonuniformity, and aspect ratio on accuracy for different cell types with various type of deviation from the ideal shape. Additionally, the orientation of the skewed, nonorthogonal, and nonuniform faces with respect to the main axes of the solution gradients will also be studied in detail. Despite all that, we can still conclude that it makes sense to optimize the mesh, as it pays back in higher accuracy for the same number of cells.

The influence of boundary conditions was not studied in this article because in most cases the number of cells with some boundary faces is much smaller than the number of internal cells and they were not considered essential to the main goal of the work. In addition, they were applied consistently for all cases in Section 4 and they could not cause the difference in the measured discretization error. The effects of the blended discretization schemes were also not considered essential, because most of the modern schemes introduce a small amount of numerical diffusion in the solution and therefore perform similarly to the studied linear interpolation scheme.

Finally, it remains to say that realistic meshes for computational domains of industrial interest will contain various types of cells and more complex solution forms. Thus, the conclusions of this study can still be used as a guideline for creation of optimal meshes in general.

REFERENCES

1. H. W. Dandekan, V. Hlavacek, and J. Degreve, Explicit 3D Finite-Volume Method for Simulation of Reactive Flows Using a Hybrid Moving Adaptive Grid, *Numer. Heat Transfer B*, vol. 24, pp. 1–29, 1993.
2. D. N. Pope and G. Gogos, A New Multicomponent Diffusion Formulation for the Finite-Volume Method: Application to Convective Droplet Combustion, *Numer. Heat Transfer B*, vol. 48, pp. 213–233, 2005.
3. B. Mondal, S. C. Mishra, P. Asinari, and R. Borchiellini, Analysis of a Localized Fire in a 3-D Tunnel Using a Hybrid Solver: Lattice Boltzmann Method, and a Fully Explicit Upwind Scheme, *Numer. Heat Transfer A*, vol. 53, pp. 392–417, 2008.
4. S. Kang and Y. Kim, Parallel Unstructured-Grid Finite-Volume Method for Turbulent Nonpremixed Flames Using the Flamelet Model, *Numer. Heat Transfer B*, vol. 43, pp. 525–547, 2003.

5. S. Kang and Y. Kim, Pressure-Based Unstructured-Grid Finite-Volume Method for Simulating Laminar Reacting Flows, *Numer. Heat Transfer B*, vol. 41, pp. 53–72, 2002.
6. K. Guedri, A. M. Abbasi, N. M. Borjini, K. Halouani, and R. Said, Application of the Finite-Volume Method to Study the Effects of Baffles on Radiative Heat Transfer in Complex Enclosures, *Numer. Heat Transfer A*, vol. 55, pp. 780–806, 2009.
7. R. Das, S. C. Mishra, and R. Uppaluri, Multiparameter Estimation in a Transient Conduction-Radiation Problem Using the Lattice Boltzmann Method and the Finite-Volume Method Coupled with the Genetic Algorithms, *Numer. Heat Transfer A*, vol. 53, pp. 1321–1338, 2008.
8. M. Ko and N. K. Anand, Three-Dimensional Combined Convective-Radiative Heat Transfer over a Horizontal Backward-Facing Step-A Finite-Volume Method, *Numer. Heat Transfer A*, vol. 54, pp. 109–129, 2008.
9. F. Asllanaj, V. Feldheim, and P. Lybaert, Solution of Radiative Heat Transfer in 2-D Geometries by a Modified Finite-Volume Method Based on a Cell Vertex Scheme Using Unstructured Triangular Meshes, *Numer. Heat Transfer B*, vol. 51, pp. 97–119, 2007.
10. W. Tian and W. K. S. Chiu, A Two-Dimensional Scheme for Axisymmetric Radiative Heat Transfer Using the Finite-Volume Method, *Numer. Heat Transfer B*, vol. 47, pp. 199–211, 2005.
11. J. C. Chai, One-Dimensional Transient Radiation Heat Transfer Modeling Using a Finite-Volume Method, *Numer. Heat Transfer B*, vol. 44, pp. 187–208, 2003.
12. J. C. Chai, J. P. Moder, and K. C. Karki, A Procedure for View Factor Calculation Using the Finite-Volume Method, *Numer. Heat Transfer B*, vol. 40, pp. 23–35, 2001.
13. M. Y. Kim, S. W. Baek, and J. H. Park, Unstructured Finite-Volume Method for Radiative Heat Transfer in a Complex Two-Dimensional Geometry with Obstacles, *Numer. Heat Transfer B*, vol. 39, pp. 617–635, 2001.
14. J. Liu, H. M. Shang, and Y. S. Chen, Parallel Simulation of Radiative Heat Transfer Using an Unstructured Finite-Volume Method, *Numer. Heat Transfer B*, vol. 36, pp. 115–137, 1999.
15. G. D. Raithby, Discussion of the Finite-Volume Method for Radiation, and its Application Using 3D Unstructured Meshes, *Numer. Heat Transfer B*, vol. 35, pp. 389–405, 1999.
16. J. Y. Murthy and S. R. Mathur, Radiative Heat Transfer in Axisymmetric Geometries Using an Unstructured Finite-Volume Method, *Numer. Heat Transfer B*, vol. 33, pp. 397–416, 1998.
17. E. H. Chui and G. D. Raithby, Computation of Radiant Heat Transfer on a Nonorthogonal Mesh Using the Finite-Volume Method, *Numer. Heat Transfer B*, vol. 23, pp. 269–288, 1993.
18. C. Beckermann and T. F. Smith, Incorporation of Internal Surface Radiant Exchange in the Finite-Volume Method, *Numer. Heat Transfer B*, vol. 23, pp. 127–133, 1993.
19. J. R. Pacheco, A. Pacheco-Vega, T. Rodić, and R. E. Peck, Numerical Simulations of Heat Transfer and Fluid Flow Problems Using an Immersed-Boundary Finite-Volume Method on Nonstaggered Grids, *Numer. Heat Transfer B*, vol. 48, pp. 1–24, 2005.
20. K. Slimi, L. Zili-Ghedira, S. Ben Nasrallah, and A. A. Mohamad, A Transient Study of Coupled Natural Convection and Radiation in a Porous Vertical Channel Using the Finite-Volume Method, *Numer. Heat Transfer A*, vol. 45, pp. 451–478, 2004.
21. P. J. Zwart, G. D. Raithby, and M. J. Raw, Integrated Space-Time Finite-Volume Method for Moving Boundary Problems, *Numer. Heat Transfer B*, vol. 34, pp. 257–270, 1998.
22. S. Muzaferija and M. Peric, Computation of Free-Surface Flows Using the Finite-Volume Method and Moving Grids, *Numer. Heat Transfer B*, vol. 32, pp. 369–384, 1997.
23. J. L. The, G. D. Raithby and G. D. Stubley, Surface-Adaptive Finite-Volume Method for Solving Free Surface Flows, *Numer. Heat Transfer B*, vol. 26, pp. 367–380, 1994.

24. Y. N. Jeng and J. L. Chen, Geometric Conservation Law of the Finite-Volume Method for the SIMPLER Algorithm and a Proposed Upwind Scheme, *Numer. Heat Transfer B*, vol. 22, pp. 211–234, 1992.
25. J. Shim, P. Dutta, and C. F. Ivory, Finite-Volume Methods for Isophoretic Separation in Microchannels, *Numer. Heat Transfer A*, vol. 52, pp. 461–461, 2007.
26. P. J. Oliveira, On the Numerical Implementation of Nonlinear Viscoelastic Models in a Finite-Volume Method, *Numer. Heat Transfer B*, vol. 40, pp. 283–301, 2001.
27. J. H. Ferziger and M. Perić, *Computational Methods for Fluid Dynamics*, 2d ed., pp. 67–256, Springer-Verlag, Berlin-New York, 1995.
28. H. K. Versteeg and W. Malalasekera, *An Introduction to Computational Fluid Dynamics: The Finite Volume Method*, chap. 5, Addison-Wesley, Reading, MA, 1996.
29. S. Dong, H. Meng, and R. O. Fox, Application of a Fractional-Step Scheme and Finite-Volume Method for Simulating Flow Past a Surface-Mounted Mixing Tab, *Numer. Heat Transfer A*, vol. 41, pp. 469–490, 2002.
30. Ž. Lilek, S. Muzaferija, M. Perić, and V. Seidl, An Implicit Finite-Volume Method Using Nonmatching Blocks of Structured Grid, *Numer. Heat Transfer B*, vol. 32, pp. 385–401, 1997.
31. C. H. Marchi and C. R. Maliska, Nonorthogonal Finite-Volume Method for the Solution of all Speed Flows Using Co-located Variables, *Numer. Heat Transfer B*, vol. 26, pp. 293–311, 1994.
32. H. Jasak, Error Analysis and Estimation in the Finite Volume Method with Applications to Fluid Flows, Ph.D. thesis, Imperial College, London, UK, 1996.
33. S. Muzaferija, Adaptive Finite Volume Method for Flow Prediction Using Unstructured Meshes and Multigrid Approach, Ph.D. thesis, Imperial College, London, UK, 1994.
34. L. Davidson, A Pressure Correction Method for Unstructured Meshes with Arbitrary Control Volumes, *Int. J. Numer. Meth. Fluids*, vol. 22, pp. 265–281, 1996.
35. C. R. Maliska, J. Flávio, and V. Vasconcellos, An Unstructured Finite Volume Procedure for Simulating Flows with Moving Fronts, *Comput. Methods Appl. Mech. Eng.*, vol. 182, pp. 401–420, 2000.
36. J. K. Dukowicz, M. C. Cline, and F. L. Addesso, A General Topology Godunov Method, *J. Comput. Phys.*, vol. 82, pp. 29–63, 1989.
37. A. Dalal, V. Eswaran, and G. Biswas, A Finite-Volume Method for Navier-Stokes Equations on Unstructured Meshes, *Numer. Heat Transfer B*, vol. 54, pp. 238–259, 2008.
38. H. Jasak and A. D. Gosman, Residual Error Estimate for the Finite-Volume Method, *Numer. Heat Transfer B*, vol. 39, pp. 1–19, 2001.
39. H. Jasak, and A. D. Gosman, Automatic Resolution Control for the Finite-Volume Method, Part 1: A-Posteriori Error Estimates, *Numer. Heat Transfer B*, vol. 38, pp. 237–256, 2000.
40. F. Juretic, Error Analysis in Finite Volume CFD, Ph.D. thesis, Imperial College London, London, UK, 2004.
41. M. A. Martins, R. M. Valle, L. S. Oliveira, and D. Burgarelli, Error Estimation and Adaptivity for Finite-Volume Methods on Unstructured Triangular Meshes: Elliptic Heat Transfer Problems, *Numer. Heat Transfer B*, vol. 42, pp. 461–483, 2002.
42. H. Jasak, and A. D. Gosman, Automatic Resolution Control for the Finite-Volume Method, Part 2: Adaptive Mesh Refinement and Coarsening, *Numer. Heat Transfer B*, vol. 38, pp. 257–271, 2000.
43. H. Jasak, and A. D. Gosman, Automatic Resolution Control for the Finite-Volume Method, Part 3: Turbulent Flow Applications, *Numer. Heat Transfer B*, vol. 38, pp. 273–290, 2000.

44. C. D. Perez-Segarra, C. Farre, J. Cadafalch, and A Oliva, Analysis of Different Numerical Schemes on the Resolution of Convection-Diffusion Equations Using Finite-Volume Methods on Three-Dimensional Unstructured Grids, Part I: Discretization Schemes, *Numer. Heat Transfer B*, vol. 49, pp. 333–350, 2006.
45. C. Farre, C. D. Perez-Segarra, M. Soria, and A. Oliva, Analysis of Different Numerical Schemes on the Resolution of Convection-Diffusion Equations Using Finite-Volume Methods on Three-Dimensional Unstructured Grids, Part II: Numerical Analysis, *Numer. Heat Transfer B*, vol. 49, pp. 351–375, 2006.
46. N. Taniguchi and T. Kobayashi, Finite Volume Method on the Unstructured Grid System, *Comput Fluids*, vol. 19, pp. 287–295, 1991.
47. N. Taniguchi, C. Arakawa, and T. Kobayashi, Construction of a Flow-Simulating Method with Finite Volume Based on a Voronoi Diagram, *JSME Int. J.*, vol. 34, pp. 18–23, 1991.
48. J. F. V. De Vasconcellos and C. R. Maliska, A Finite-Volume Method Based on Voronoi Discretization for Fluid Flow Problems, *Numer. Heat Transfer B*, vol. 44, pp. 319–342, 2004.
49. S. V. Patankar, *Numerical Heat Transfer and Fluid Flow*, pp. 143–146, Hemisphere, Washington D.C., 1980.
50. H. Schlichting and K. Gersten, *Boundary Layer Theory*, 8th ed., pp. 177–180, Springer-Verlag, Berlin Heidelberg, 2000.